Urea-Modified Self-Assembling Peptide Amphiphiles That Form Well-Defined Nanostructures and Hydrogels for Biomedical Applications

Huihua Xing, [a] Alison Rodger, [b] Jeffrey Comer, [c] Agustín S. Picco, [d] Cristián Huck-Iriart, [e] Edward L. Ezell, [f] Martin Conda-Sheridan [a]*

Email: martin.condasheridan@unmc.edu

Phone: +1 402-559-9361

KEYWORDS: hydrogen bonding, peptide amphiphiles, nanostructures, self-assembly, hydrogel, 3D cell culture

[[]a] College of Pharmacy, University of Nebraska Medical Center, Omaha, NE 68198, USA

[[]b] School of Natural Sciences, Macquarie University, Sydney, NSW 2109, Australia

^[c] Department of Anatomy and Physiology, Kansas State University, Manhattan, KS 66506, USA

^[d] Instituto de Investigaciones Fisicoquímicas Teóricas y Aplicadas, INIFTA-CONICET-UNLP, Diagonal 113 and Calle 64, La Plata (1900), Argentina

^[e] Instituto de Tecnologías Emergentes y Ciencias Aplicadas (ITECA), UNSAM-CONICET, Escuela de Ciencia y Tecnología (ECyT), Laboratorio de Cristalografía Aplicada (LCA), Campus Miguelete, 1650) San Martín Buenos Aires, Argentina.

^[f] Eppley Institute for Research in Cancer, University of Nebraska Medical Center, Omaha, NE 68198, USA

ABSTRACT

Hydrogen bonding plays a critical role in the self-assembly of peptide amphiphiles (PAs). Herein, we studied the effect of replacing the amide linkage between the peptide and lipid portions of the PA with a urea group, which possesses an additional hydrogen bond donor. We prepared three PAs with the peptide sequence Phe-Phe-Glu-Glu (FFEE): two are amide-linked with hydrophobic tails of different lengths and the other possesses an alkylated urea group. The differences in the self-assembled structures formed by these PAs were assessed using diverse microscopy, NMR, and dichroism techniques. We found that the urea group influences the morphology and internal arrangement of the assemblies. Molecular dynamics simulations suggest that there are about 50% more hydrogen bonds in nanostructures assembled from the urea-PA than those assembled from the other PAs. Furthermore, in-silico studies suggest the presence of urea- π stacking interactions with the phenyl group of Phe, which results in distinct peptide conformations in comparison to the amide-linked PAs. We then studied the effect of the urea modification on the mechanical properties of PA hydrogels. We found that the hydrogel made of the urea-PA exhibits increased stability and self-healing ability. In addition, it allows cell adhesion, spreading, and growth as a matrix. This study reveals that the inclusion of urea bonds might be useful in controlling the morphology, mechanical and biological properties of selfassembled nanostructures and hydrogels formed by the PAs.

Introduction

The spontaneous organization of molecules (self-assembly) enables the bottom-up fabrication of supramolecular structures with diverse and unprecedented properties. ¹⁻³ Such structures can have applications in the energy, chemical, biomedical, and pharmaceutical industries. ⁵⁻⁷ Amino acids are one of the most attractive building blocks for such systems due to the chirality and physicochemical diversity of their side chains, which allows the control of the stereochemistry, morphology, and electronic properties of the obtained nanostructures. ^{1, 4, 8-11} An intriguing class of amino acid-derived molecules are the peptide amphiphiles (PAs): short peptide sequences covalently conjugated to an alkyl tail. PAs can assemble into nanostructures with diverse applications. ^{4, 5, 7, 11, 12} To design PA nanostructures tailored to specific applications, it is key to understand and exploit the intermolecular interactions involved in PA assembly.

A seminal report by Hartgerink and co-workers studied the role of hydrogen bonds (H-bonds) in the self-assembly of PAs. They found that H-bonds near the core of the nanostructure dictated the morphology of the assemblies. Later, Stupp's group illustrated the correlation between H-bonding and nanofibers-stiffness. His group found that PAs forming twisted or disordered β -sheets have weaker H-bonding patterns, which result in low stiffness, when compared to PAs that form ordered β -sheets. H-bonding also plays an important role in the length and stability of PA nanofibers. H-bonding also plays showed that strong intermolecular bonds decrease the cell death caused by the disruptive interaction between PAs and cell membrane. He is the strong intermolecular bonds decrease the cell death caused by the disruptive interaction between PAs and cell membrane.

Furthermore, PA nanofibers can be formulated into hydrogels with diverse biomedical applications including drug delivery¹⁸⁻²⁰ and tissue engineering.²¹⁻²³ Stendahl et al. have demonstrated that the strength and stiffness of PA nanofibers and the presence of crosslinks are critical to tune the mechanical properties of these gels.²⁴ Although the importance of H-bonding in self-assembly has been clearly established, strategies to strengthen H-bonding have been limited to exchanging or adding/removing amino acids residues. Thus, it is desirable to design a strategy that allows to tune the properties of PA nanostructures while minimally modifying the peptide backbone.

Urea is used to unfold proteins due to its strong H-bonding properties.²⁵ Earlier reports from Fowler, Lauher and their groups studied the self-assembling properties of urea-

modified dicarboxylic acids. $^{26-28}$ They found those molecules formed self-assembled systems ("molecular solids") that display organized β -sheet networks – by themselves and also in combination with a second molecule. Later, Drummond and co-workers prepared N-alkyl substituted ureas that form thermodynamically stable lyotropic liquid crystalline phases. 29 Notably, the melting point of the assemblies was independent of the alkyl chain length due to the urea H-bond interactions dominating the thermodynamics. 29 The group of Feringa designed a chiral bis(urea) amphiphile, whose morphology can be programmed to assemble into flat sheets, helical ribbons, and twisted ribbons. 30 These nanostructures also showed thermo-responsive behavior. 31

Among the common amino acids that can be included in the PAs' molecular structure, phenylalanine (F), tyrosine (T), and tryptophan (W) are intriguing to study because their aromatic side chains can participate in π - π interactions. The literature shows that the presence of aromatic side chains affects the supramolecular morphology, and the physicochemical and biological properties of peptide-based assemblies. The interplay of π - π interactions, hydrophobic collapse, and H-bonds can be used to create twisted ribbons, ananotubes, and nanobelts. In the field of PAs, Guler et al. prepared and characterized the PA of formula $[C_{12}]F_2H_2$ ($[C_{12}]=[C_{12$

Based on these precedents, we decided to investigate the effect of adding a urea group into the molecular structure of Phe-based PAs. Our hypothesis was that the presence of the urea functionality would influence the physico-chemical and biological behavior of the PA nanostructures due to the additional H-bonding capability. Indeed, molecules containing urea groups can form bifurcated H-bonds involving the two NH donors of one molecule and the carbonyl oxygen of the next molecule (**Figure 1A**).⁴⁵

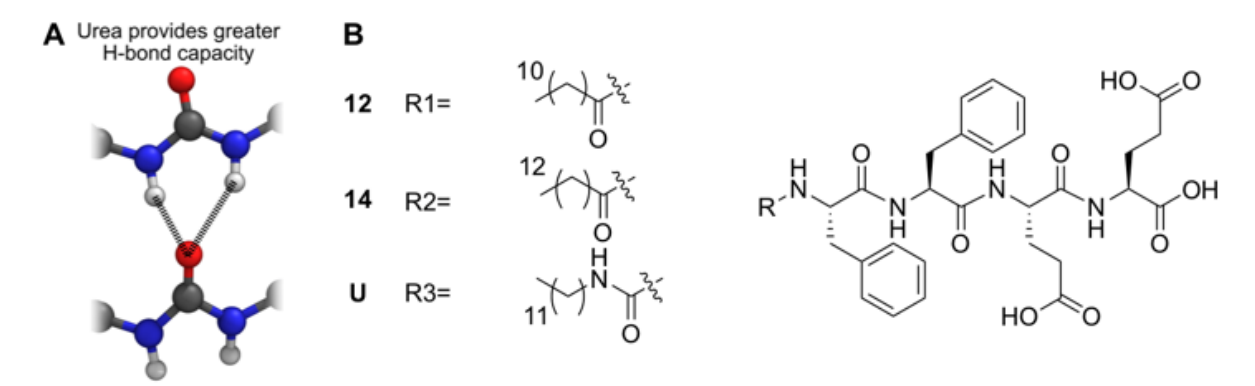


Figure 1: A) Urea modified PA backbone (lines indicate H-bonds). B) Chemical structures of 3 PAs, from top to bottom: PA **12**, PA **14**, and PA **U**.

Figure 1B shows a urea-modified PA of formula [C₁₂]UF₂E₂ (**U**, the urea group was placed between the lipid and the peptide portion). Three controls were designed to distinguish the effect of H-bonds and van der Waals interactions. First, we prepared $[C_{12}]F_2E_2$ (12), which has a lauric acid tail containing the same number of carbon atoms on the alkyl chain as U. Next, we designed $[C_{13}]F_2E_2$ (13), which contains the same number of carbon atoms adjacent to the peptide sequence. Finally, we prepared [C₁₄]F₂E₂ (14) with a myristic acid segment that possesses the same number of heavy (nonhydrogen) atoms adjacent to the peptide sequence. We studied the supramolecular morphology of the nanostructures using transmission electron microscopy (TEM) and atomic force microscopy (AFM), and the behavior of the nanostructures in the solution was obtained by Small-angle X-ray Scattering (SAXS). Then, we used NMR, infrared absorbance (IR), linear dichroism (LD), and circular dichroism (CD) to understand the molecular arrangement. The experimental results were supported by computational models that give a detailed picture of the nanostructures at the atomic level, including the number of H-bonds per PA molecule within nanostructures and the orientation of the Phe side chains helping us to interpret the experimental results. Rheometric studies were performed to study the effect of H-bonds supplied by the urea motif on the mechanical properties of PA hydrogel, and cell viability experiments were performed to demonstrate the interaction between PA materials and cells.

Experimental section

Synthesis and characterizations: All PAs were synthesized using standard Fmoc solid-phase peptide chemistry on a 0.3 mmol scale on Fmoc-Glu(OtBu)-Wang Resin. The

couplings of amino acids and hydrophobic tails were done following our previous paper.⁴⁶ **U** was synthesized by coupling the peptide segment to a dodecyl isocyanate molecule (8 equivalent) with DMSO/DMF=1/1. The obtained molecules were purified and characterized as reported but with a solvent mixture of acetonitrile and water; both containing 0.1% ammonium.^{46, 47} The mass was confirmed by MALDI (Bruker Autoflex maX). The organic solvent was removed, the samples were frozen and lyophilized (FreeZone, Labconco) after adjusting pH to 7.0 (0.1 M HCl and NaOH).

Preparation of Molecular Assemblies: Lyophilized PAs were dissolved in HPLC grade water/buffer to the concentration required by the experiment (usually 1 mg/mL, see below). The samples were annealed at 80°C for 2 h (isotemp hot plate, Fisher Scientific or spectrometer heating unit), and slowly cooled to room temperature and aged before testing. The final pH was confirmed by a pH meter.

Atomic Force Microscopy (AFM): PA samples (1 mg/mL) were deposited on aminopropyl silatrane (APS) mica and scanned according to the protocol in our previous paper.⁴⁷

Transmission Electron Microscopy (TEM): The PAs were prepared to give a final concentration of 1 mg/mL and aged for the required time before the experiments. The operation followed the protocol described in our previous work.⁴⁶

Small-angle X-ray Scattering (SAXS): SAXS data were collected on BioSAXS/HP-Bio beamline ID7A at Cornell High-Energy Synchrotron Source (CHESS). The X-ray beam was collimated to $250 \times 250 \ \mu m$ and the sample-to-detector distance was ~2 m. PA solutions prepared at 5 mg/mL were aged overnight before the scanning. The data was collected by a Dectris Eiger 1M detector.

Infrared absorbance (IR): IR spectra were measured in solution, with a Jasco FTIR-6700 spectrometer (Hachioji, Japan) with a TGA detector, or as fibers deposited on Glad Press'n Seal PE film that has been oxidized in a Plasma Asher for 30 s and stretched two-fold further in the manufacturer's stretch direction, with a Jasco FVS-6000 vibrational circular dichroism instrument (Hachioji, Japan) with an MCT detector.

Circular Dichroism (CD): CD studies were performed in a J-815 Jasco Circular Dichroism Spectropolarimeter (Easton, MD) or a Jasco J-1500 spectropolarimeter (Hachioji, Japan) with a 0.1 mm quartz demountable or 1 mm and 1 cm fixed pathlength

cuvette from 25–90 °C. The parameter sets used were either a wavelength range of 190–300 nm with a scan speed of 50 nm/min in continuous scanning mode, a data pitch of 0.1 nm, a response time of 1 second, and a bandwidth of 1 nm or 180–300 nm, 100 nm/min, 0.2 nm, 1 s, and 2 nm respectively. Water was used as the reference (blank), and five scans were recorded for each PA. PA solutions were prepared at various concentration (0.1 mg/mL – 1 mg/mL) based on the experiment's requirements.

Linear Dichroism (LD): LD was measured as a 1 mm path length Couette flow cell ⁴⁸ using the same parameters as the 100 nm/min CD measurements and rotating at 1000 rpm for the sample measurement and 0 rpm for the baseline measurement. PA solutions were prepared at 0.1 mg/mL, followed by the annealing step.

Nuclear magnetic resonance (NMR): Data was obtained on a Bruker 600 MHz Avance III HD spectrometer equipped with a 5mm 3-channel (CHN) cryoprobe and Z-gradient pulsing. Samples of 12 and U (10 mg/mL) were dissolved in H₂O/D₂O (90%:10%) and maintained at 25 °C during data acquisition.

Peptide Gelation: A 10 mg/mL solution of PA was prepared by dissolving the lyophilized powder in HPLC grade water and sonicated to obtain the clear solution. After annealing at 80°C, cooled to room temperature, CaCl₂ solution (160 mM) was added to promote the gelation.

Scanning Electron Microscopy (SEM) characterization of hydrogel: PA solutions were prepared at 10 mg/mL at neutral pH, annealed and aged overnight. 160 mM CaCl₂ was added to PA solution for the gelation on the surface of a plastic coverslip. Resulted hydrogels were then dried under vacuum. Samples were imaged at 30 kV in an FEI Quanta 200 SEM.

Rheometry study for hydrogels: Rheological measurements were taken by a hybrid rheometer DISCOVERY HR-2 (TA Instruments) with a flat plate, 20MM. Approximately 300 μL of gel solution was placed on the steel parallel plate geometry and let for 10 mins for gelation. A strain sweep was performed at 25 °C and 10 rad/s from 0.01% to 100% strain. 0.1% strain was selected to perform the frequency sweep ranging from 0.1 to 100 rad/s. Time sweep was performed using 10 rad/s and 0.1%/100% strain. In the shear and recovery test, after 15 mins equilibrium with 0.1% strain, 100% strain was applied to the

gel for 5 mins to break the gel, followed by reducing the strain again to 0.1% over 20 mins. The phase angle was kept below 90°.

Metabolism study: For the human serum stability studies, PAs (2 mg/mL) were incubated in serum (50 v/v%) over 24 h in a shaking incubator (37 °C and 75 rpm). At selected time intervals 0, 15, 45, 90, 120, 720, and 1440 min, 100 μ L aliquots were taken to be heated to 80 °C for 1 min to destroy the proteins subtracted and quenched with 100 μ L of methanol (containing a standard compound) and centrifuged at 12,000 rpm (Eppendorf Centrifuge, USA) for 5 min. An aliquot of the supernatant (70 μ L) was removed for analysis using HPLC. The stability results were expressed as % of PA remaining vs time. The calculations were performed as % parent remaining at select time points relative to 0 min (100% parent).

Cell culture: All cell lines were cultured using ATCC protocols and passages 3–8 were used for all of the experiments. The cytotoxicity was accessed by XTT and LDH release (Promega CytoTox 96® Non-Radioactive Cytotoxicity Assay) tests.

2D cell culture: The plate was treated with 0.01% (w/v) poly-D-lysine for 1 d at room temperature, followed by washing three times with H₂O. To make an evenly distributed hydrogel, as well as avoid bubbles during the procedure, we made the hydrogel directly inside the plate. A thin layer of 160 mM CaCl₂ solution was added on the bottom, then the PA solution (10 mg/mL) was added on the top to form a thin layer of hydrogel. The solution residue was removed. The PA-coating plate was incubated at 37°C overnight. SH-SY5Y suspension of density 5×10^4 was seeded on the PA-coating treated plate and were incubated for 48 hours. Calcein AM and Hoechst 33342 were diluted with PBS to make a final 1 μ M mixture solution. The cells were stained by the mixture for 15 mins at 37°C. The dye was removed, and PBS was added for 60 mins before imaging (Zeiss LSM 800 with Airyscan Confocal Microscope). The spreading area and perimeter of cells on each PA hydrogel were measured by Fiji ImageJ, and at least 25 cells were analyzed. Statistical analysis was performed using Prism 9. Other alternatives for culture can be found in SI.

3D cell culture: Cell suspension of density 5×10^4 was mixed with PA solution (10 mg/mL) and added to the plate which was covered by 160 mM CaCl₂ solution. The residue

of the salt solution was removed and washed with PBS. The medium was added to cover the gels and the plate was incubated at 37°C with 5% CO₂.

Results and discussion

1. Morphology of PA nanoassemblies

The PAs were synthesized, and the nanostructures prepared as detailed in the experimental section. The micrograph of 12 (Figure 2A) shows wide nanoribbons (width = 95 ± 31 nm). Other supramolecular structures, possible nanotubes, are observed by TEM (Figure S1). The nanoribbons flip, tilt and entangle with other nanoribbons indicating a high degree of flexibility. Some of these nanostructures seem coiled while others are flat. Similar nanostructures were observed by Cui et al., who found that narrower ribbons stacked together to form multi-layered structures, which they called nanobelts.⁴² Interestingly, molecule 13 formed nanoribbons with less twisting and smaller width; 25 ± 5 nm (Figure S2). Burnett et al. have reported that an odd number of carbon atoms in the alkyl chains (next to the aromatic component) has an influence on twisting.⁴⁹ This could be an explanation for the observed morphology, which is different from 12 and 14. Thus, due to the unclear odd-even effects, only 12, 14, and U were studied in this report. 50 Molecule **14** assembled into similar nanostructures (width = 91 ± 21 nm, **Figure 2B**) but present flat construction. The micrographs show stacks of belts (clear images can be seen in AFM and SI ref to figs), which cause large standard deviations (STD) on the measured widths. Figures S3A, B shows separated (individual) twisted ribbons at the end of the nanobelt, indicating the transition of these supramolecular structures. Intriguingly, U (Figure 2C) forms highly twisted and well-defined nanoribbons when compared with 12 and 14. Figure S4 shows the presence of single and multi-strand ribbons (average width = 20 ± 3 nm), which are composed of two or more single ribbons.

AFM also shows that **12** forms nanobelts with widths of 117.9 ± 26.0 nm and thicknesses of 12 ± 1 nm (**Figure 2D**). The AFM height profiles suggest the coexistence of stacked flat belts, coiled belts, and fused belts (these structures may be precursors to nanotubes, **Figure S5**). Molecule **14** assembles into flat nanobelts that are 85 ± 35 nm wide and 20 \pm 3 nm thick (**Figure 2E**). The data suggest **14** is composed of additional stacks of nanobelts when compared with **12**. AFM height profiles further suggest the notion of a

multi-layered nanobelt pattern for **14** (**Figure S6**). The thicknesses of nanostructures formed by **12** and **14** are greater than those reported for a PA with an interlocked peptide bilayer (\approx 4.7 nm),⁴² further endorsing the notion of stacks. In contrast, **U** shows fairly uniform-sized twisted structures (**Figure S7**, average width = 14 ± 1 nm, calculated by the equation: W = S sin γ , details shown in SI). Thus, the AFM and TEM results (both with dried samples) are consistent with each other: **12** and **14** form wide nanobelts while **U** forms twisted ribbons. **Figure S8** shows the fiber stiffness obtained by AFM Quantitative Nanomechanics (QNM), which **12** and **14** possess higher stiffness than **U**. However, the twisting of **U** and stacking structures of **12** and **14** influence the data.

As reported by the Nyrkova's and Stupp's groups, twisted β -sheets laterally stack into linear structures. Thus, a flat nanobelt can be obtained when there is sufficient lateral adhesion energy to untwist PA sheets, but this effect depends on the concentration and complementary interactions of the peptide side chains.³² In the case of **12** and **14**, at neutral pH, the COOH groups on the glutamate side chains are partly deprotonated (there is a pK_a shift due to proximity of the carboxylates in the assembly).⁵¹ The hydrophobic collapse of alkyl tails and π stacking compensate the elastic penalty of untwisting peptide sheets, resulting in 2D structures via lateral growth.⁴² A coiling tape mechanism and helical lamellar mechanism of aromatic PAs have been studied by others.³² Compared to 12, 14 shows a greater amount of planar multi-layered nanobelts than single coiled bilayer nanobelts, owing to the stronger hydrophobic collapse provided by longer alkyl tail. Clear stacking can be seen in the TEM and AFM images (Figure 2B and E, layers indicated by arrows). However, **U** assembles into narrower well-twisted ribbons, which may be due to the limitation of lateral growth by the helicity. 32 Considering that **U** has a similar alkyl tail length and the same number of aromatic side chains as the other PAs, the dramatic difference in morphology can be ascribed to the urea motif. The critical lateral growth promotor, π stacking, is affected by the urea motif, resulting in twisted peptide sheets. This hypothesis is supported by computational simulations (see below in Section 3). A plausible explanation for this effect is that urea increases the stability of the assemblies, discouraging untwisting and the subsequent formation of larger nanostructures.

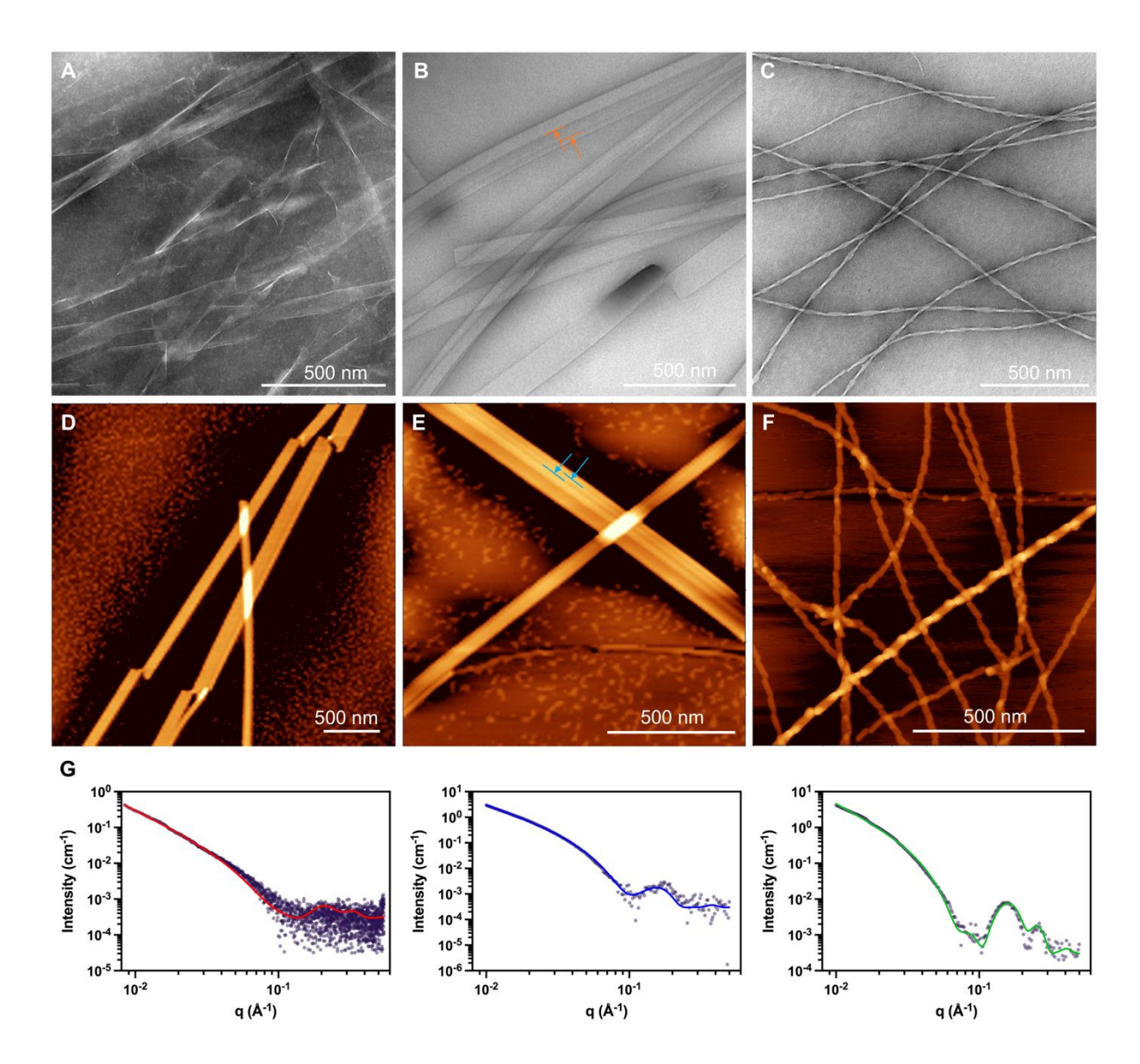


Figure 2. Morphology of PAs assembled in water at 1 mg/mL aged for 1 day. The left panels (A and D) show the nanostructures of 12, while the middle panels (B and E) show the nanostructures of 14, and the right panels (C and F) show the nanostructures of U (scale bars 500 nm). The light area shows greater height compared to the dark area, which indicates the multi-layered structures caused by twisting or stacking. G) SAXS patterns in the log-log scale of, from left to right, PA 12, 14, and U respectively.

Table 1. Nanostructure's width, height, and standard deviation measured from TEM and AFM images.

	TEM (nm)	AFM (nm)	
	Width	Width	Height
12	95 ± 31	118± 26	12 ± 1
14	91 ± 21	85 ± 35	20 ± 3
U	20 ± 3	17± 3	5 ± 0

The drying process in both TEM and AFM may affect the morphology of the samples, such as aggregation and/or a stepwise increase in thickness due to the changes in the concentration of the molecules and the changes in surface tension of the solvents. Furthermore, the morphology observed by AFM can be affected by the sample-mica interaction. To assess that no artifacts were present, we studied the PA samples in solution. The SAXS data show that $\bf U$ exhibits more and clear features (e.g. the bumps above 0.1 Å) than the other two PAs. Based on the trend at low angles (slope ~ -2) of the SAXS curves (**Figure 2G**), all PAs seem to form 2D nanostructures (i.e. lamella or wide ribbon structures). The results are compatible with the stacking of two bilayers as observed in the TEM and AFM, but with an expected smaller width (drying affect). However, clear differences can be seen between the three PAs.

A simple lamellar model was used to interpret the inner structure of the large nanostructure shown in the micrographs (twisting and curvatures of the structures were not considered). The model also accounts for the possible stacking of the lamellas. Detailed description of the model can be found in the SI. Fitted curves are shown as solid lines in **Figure 2G**. The adjusted parameters (see **Table S4**) show a molecular length (half of the thickness) inside the layer between 1.4 to 2 nm which is slightly shorter than what is expected for the fully extended molecule, suggesting an overlapping of the hydrophobic tails. The data also show transversal structure factors indicating the stacking of PA molecules with overall thickness around 6 to 9 nm. The layer thicknesses increase in the sequence **PA 12**, **14**, **U**, while the number of stackings is in order $12 < U \le 14$.

In addition, the electronic contrast increased when going from 12 to 14, allowing for better differentiation between the head and the tail of the structures. This might be a consequence of the higher hydrophobicity of 14 compared to 12. In the case of U, its highest thickness (both single-molecule and overall) may be a result of the intermolecular position shift caused by the H-bonds and potential urea- π interactions (see below for experimental and theoretical analysis). Moreover, it also exhibits an even higher electronic contrast than 12 and 14 which might be derived from the greater urea H-bonds potential when compared with the amide group, thus makes the PA head in the assemblies more compact (evidenced by the increased scattering length).

To further study the intermolecular contacts between individual PAs, 2D NMR NOESY was performed for **12** and **U** in D_2O/H_2O (data shown in **Figure S9**). Significantly more cross peaks were seen for **U** than for **12**, suggesting higher compactness (in accord with the SAXS results). The large number of cross peaks in **U** also be correlate with the observed high twisting, which positions the atoms in close proximity to each other (< 5 Å).

The morphological studies demonstrated the critical role of the urea motif in stabilizing the twisted ribbons. We speculate that urea-PA could work as a morphology tuner in a hybrid nanostructure. Thus, we studied the behavior of equimolar mixtures of **U** with **12** or 14. TEM shows the presence of U disturbs the nanobelt structures discussed above and illustrated in Figure S10 for 12 and 14, and promotes the twisting of the assemblies. This result highlights the role of the stronger H-bonding group on the nanostructures. The possible reason for these changes may be the twisting angle and weaker π - π stacking caused by the urea- π interaction. The insertion of **U** changes the twisting behavior of **12** and 14, as the angle between F-F is changed. Further, the degree of twisting is decreased when compared to **U** by itself. As described by Pashuck et al., 40 aromatic stacking rearrangement can lead to a transition from twisted to helical ribbons. Then, we studied different molar ratios of **U/12** and **U/14** to understand the relationship between the amount of **U** and the twisting behavior of the hybrid. For **12** (left panel in **Figure S11**), 3 eq. of **U** gave the most twisted morphology while the other two ratios exhibit short fibers (blue arrow). However, for **14** (right panel in **Figure S10**), 2 eq. of **U** provides the most mature nanostructures, while neither of the ratios can induces the same twisting as the **U** itself. Assuming that within the nanostructures the mixtures are homogeneous and no sections of pure U and 12 or 14 are present in an assembly, the data indicate that 0) U has a high affinity for the other peptides, 1) when the ratio of **U** is high in the mixtures, the other PAs start to become the disruptor and/or aggregate separately to form short fibers; 2) 12 takes more **U** to reach a stable morphology status but can be tuned totally by **U** when compare to 14, perhaps to its weaker intermolecular cohesion when compared to 14. Thus, a profound change in nanostructure morphology occurs only by substituting amide with urea.

2. Spectroscopic characterization of the nanostructures

We used IR to investigate the secondary structure of the fibers. All three PAs form β sheet amyloid-type fibers, (Figure 3A) as shown by their sharp peaks in the β -sheet region.^{54, 55} PAs **12** and **14** have the amide I peaks at 1632 cm⁻¹ whereas this peak in **U** is somewhat broader and weaker, occurring at 1638 cm⁻¹. The amide II bands of **12** and **14** occur at 1544 cm⁻¹, midway between published positions for oligomers (1532 cm⁻¹) and fibers (1553 cm⁻¹).⁵⁵ For **U**, this band occurs at 1564 cm⁻¹. The distinct spectrum for **U** is partly due to the presence of the urea chromophore, but the wavenumber shift to a value larger than the published value for fibers indicates a different local β-sheet fiber structure. ⁵⁶ It has been reported that a redshift occurs in the amide I region with increasing stability of the H-bonding network. However, in our case, a possible reason for the opposite shift is that individual intermolecular H-bonding is weakened by the twisted arrangement (larger intermolecular space). Meanwhile, there is still one more potential intermolecular H-bond in **U** than the other two PAs. Attenuated total reflection (ATR) solution measurements gave similar (though weaker, data not shown) spectra to the samples dried onto stretched films. Computational studies (see below) suggest **U** has 1.4 times more H-bonds than 12 and 14. In summary, 12 and 14 have uniform β -strand structures with positions consistent with an amyloid cross- β structure and no other structures; **U** has a slightly broader signature, presumably due to the addition of the urea chromophore, but it is still a very narrow band compared with normal protein IR suggesting a tight uniform β -structure.

Linear dichroism (LD) spectra (**Figure 3B**) show the presence of elongated structures immediately after annealing. Solutions of **14** were cloudy and exhibited significant scattering (sloping signals outside any absorbance band) which increased with time. Scattering for **12** and **U** was evident after 3 hours. All three samples have a small positive shoulder band at about 218 nm, a positive peak at 204 nm, and negative signals at about 190 nm. The 204 nm peak indicates the carbonyl chromophores of the amide bands are oriented along the flow direction as expected for an amyloid-type fiber. ⁵⁷⁻⁶¹ **U** also has a clear negative band at 237 nm due to a transition perpendicular to the axis of the elongated nanostructure. 3 hours later, only the 190 nm region retains an obvious negative signal for all nanostructures, though the other bands may be present under the positive scattering signal which has grown significantly, in accord with significant fibre

growth in size. The 237 nm peak seen for **U** may be related to the urea chromophore's presence, though after 3 hours, **12**, **14**, and **U** all have a very small band at \approx 232 nm, which is polarized perpendicular to the $\pi \rightarrow \pi^*$ carbonyl transition at 204 nm suggesting it relates to a coupling between phenyls and carbonyl chromophores. The absorbance (i.e. non scattering) contribution to what is measured indicates a constant amyloid- β local structure for all the fibers. Due to the lack of LD intensity at 220 nm where a positive and negative intensity LD signal cancel, no 208 nm band (which is usually seen as a dip for an alpha helical structure) and a large positive signal just above 200 nm.^{57, 62}

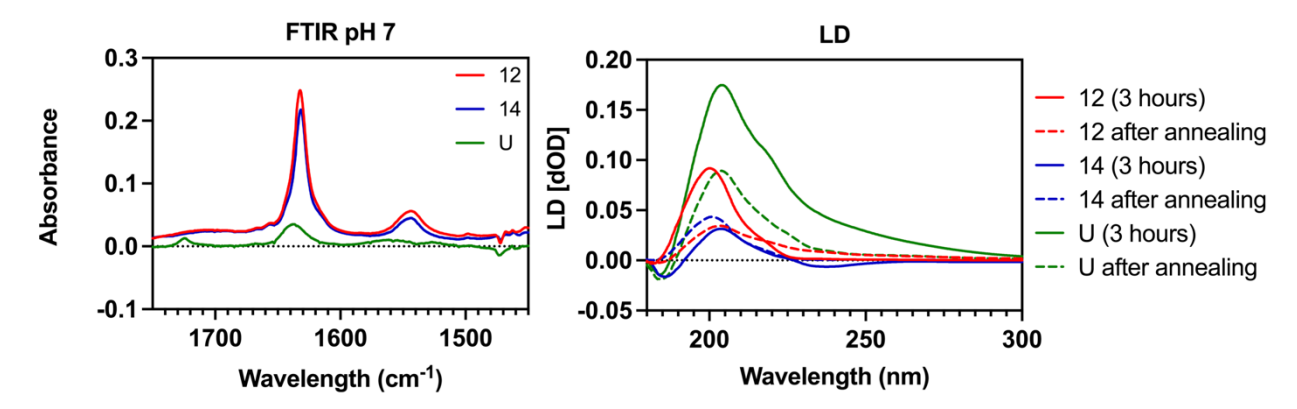


Figure 3. A) IR spectrum of the stretched films of dried samples. B) UV LD of PAs at a concentration of 0.1 mg/mL immediately after annealing and 3 hours later. All samples were prepared at pH 7.

We then measured 0.1 mg/mL PA solutions by CD with 1 mm and 1 cm path length cuvettes (see **Figure S12**), to understand the chirality of the nanostructures. The smaller path lengths showed little or no change in CD shape over time whereas the 1 cm showed variable spectra at long time which we assume to be due to larger structures being present or absent from the light beam and having very different scattering profiles overlaid on the CD spectra. The magnitudes of the spectra are all larger than normally expected for solution CD spectra suggesting contributions from chiral macrostructures as well as simple light scattering. **12** (left panel of **Figure S12**) shows similar signature peaks for the 1 mm and 1 cm pathlength cuvette spectra though gains a scattering contribution and changes to have a large negative peak at about 215 nm after a few hours. Directly after annealing, both 1 cm and 1 mm pathlength cuvettes show a 222 nm positive shoulder, a 216 nm dip in intensity (which given the absorbance is probably a negative CD signal), a 205 nm positive peak. The signs and positions are consistent with a β -sheet dominated structure. The spectra vary between the two conditions and with all repeat runs show the

same type of spectrum but at different time points. **14** (middle panel of **Figure S12**) shows the greatest difference from the **12** spectrum (immediately after annealing and even before the annealing step), and the CD signal is dominated by scattering (giving large sloping baselines). It also shows great variability with time especially in the 1 cm path length cuvette. The most striking feature about the **U** spectra, compared with the others, is that they are consistent over time (showing a small increase in intensity) and path length (right panel of **Figure S12**). Thus, the **U** fibers keep their initial local structure during the experiments. This can be explained by the fact that the stronger H-bond leads to thermodynamically favored supramolecular assembly more quickly.

The electronic CD indicates that **14** immediately forms large fibers and **12** more slowly forms the same structures (on the length scale of an electronic coupling). **12** and **U** begin with similar spectra which **U** retains (though its scattering component increases). Longer time **12** and **14** electronic CD spectra vary inconsistently which we deduce to be due to the formation of large structures which gradually precipitate to be replaced by others. After sometime , small but clear phenylalanine CD bands are evident between 260 nm and 270 nm which are negative for **12** and **14** but positive for **U** indicating opposite average F-F twist angles in the two types of structures.

3. Molecular simulations of PA assembly

The nanostructures shown in **Figure 2** are too large to be simulated at the atomic level with current technology. Nevertheless, molecular dynamics (MD) simulations can still yield information regarding how atomic-scale interactions in the PAs affect their self-assembly from monomers. We studied the self-assembly of the three PAs (**12**, **14**, **U**) in solution using a constant-pH algorithm at pH 7.4.⁶³ At the beginning of each simulation, 64 PA molecules were randomly distributed in the fully protonated (electrically neutral) state. At pH 7.4, they rapidly deprotonated while coalescing into aggregates. After about 40 ns, the average fraction of protonated Glu residues plateaued at 4–5% for all PAs, while the C-termini were almost fully deprotonated (<0.02% protonation). The final structures of the aggregates (after 65 ns) are shown in **Figure 4A–C**. The overall shape of the **U** aggregate was less spherical than the others, which may be linked to the distinct morphologies shown in **Figure 2**. Larger scale simulations to better understand this link will be pursued in future studies. After about 40 ns, the structures of the aggregates

became somewhat stable. The number of H-bonds per molecule is shown in **Figure 4D**, revealing a considerably greater (40%–60%) average number of H-bonds for the urealinked PA than for the amide-linked PAs. We expect this increase in H-bonds will translate to more stable nanostructures.

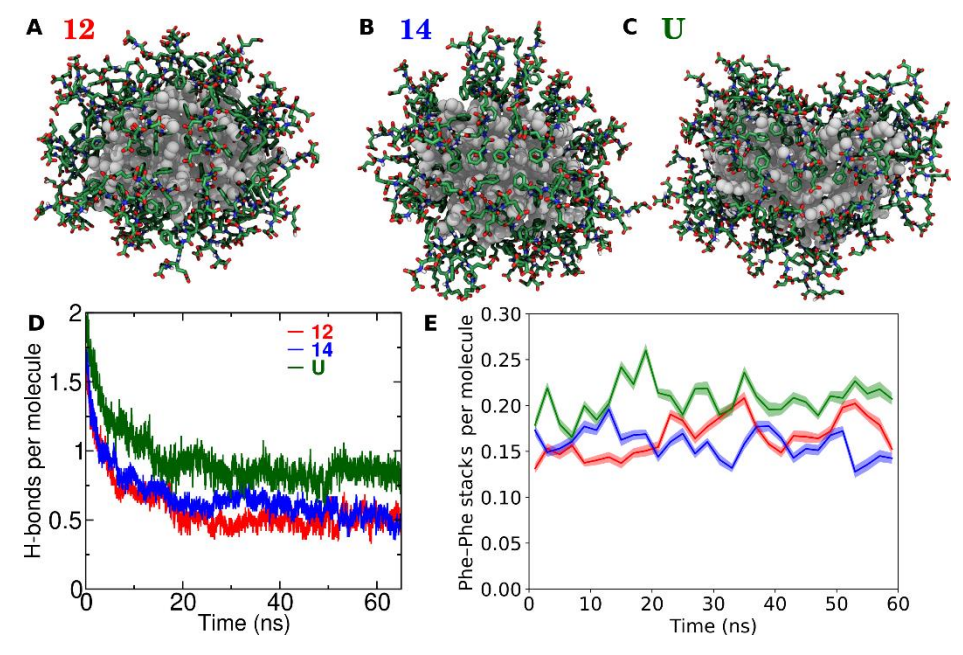


Figure 4: Molecular dynamics simulations of PA self-assembly. Structures of PA aggregates formed from 64 molecules of **12** (A), **14** (B), and **U** (C) in a constant-pH simulation. Explicit water molecules, nonpolar hydrogen atoms, and Na⁺ and Cl⁻ ions are not shown. The carbon atoms of the aliphatic and peptide portions of the PAs are shown as gray spheres and green bonds, respectively. Other colors are H, white; N, blue; O, red. The number of (D) H-bonds and E) Phe-Phe stacks per PA molecule as a function of time during the constant-pH simulation.

As exemplified in **Figure 5A**, parallel β -sheet like structures formed on the surfaces of the PA assemblies. These β -sheets are associated with H-bonds between amide/urea NH and O groups along the peptide backbone. While β -sheet structures appeared for all three PA types, the urea-linked PA (**U**) exhibited very different peptide conformations compared with the amide-linked analogs (**12** and **14**). As shown in **Figure 5B**, the β -sheets formed by **14** were relatively flat and the phenyl groups of the Phe residues pointed away from the peptide backbone. The side-to-side arrangement of the phenyl groups precluded π stacking between the PA molecules in the same sheet. Similar structures were observed for **12**. In contrast, β -sheet like assemblies of **U** exhibited frequent urea— π stacking interactions, β 4 which principally formed intramolecularly between residue Phe2

and the urea linker. This interaction, which has been identified in nature, $^{25, 65}$ is highlighted in **Figure 5C**. Owing to this interaction, the backbone of the assembled **U** molecules exhibited an $\approx 90^{\circ}$ angle between residues Phe1 and Phe2. This backbone conformation, in turn, allows π stacking of the phenyl groups.

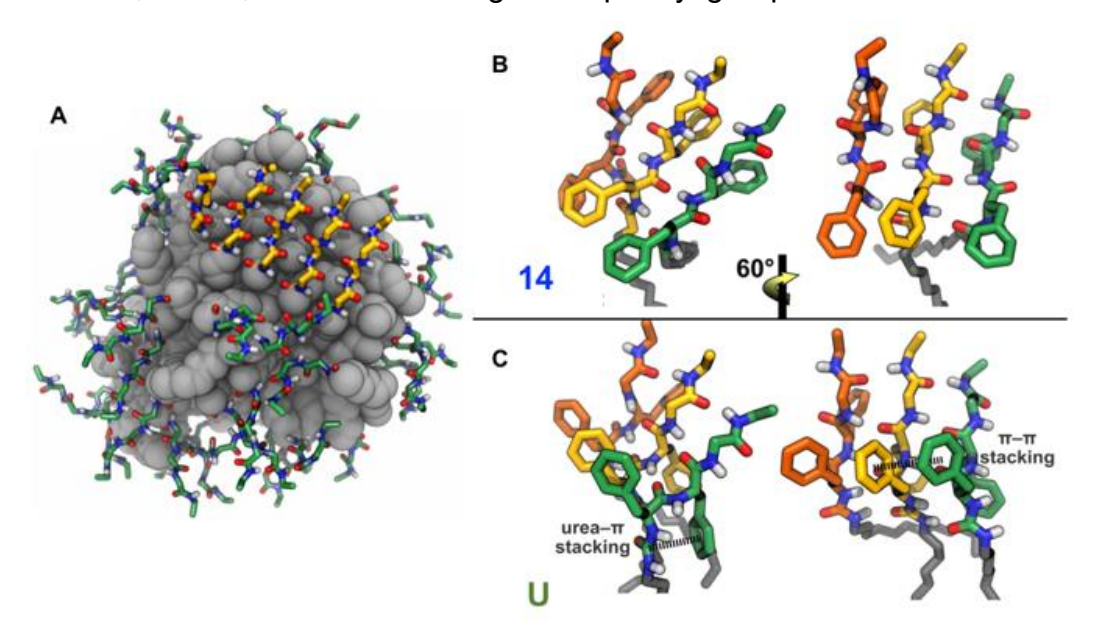


Figure 5: The urea-linked and amide-linked PAs exhibit distinct peptide conformations in molecular simulations. (A) A five-strand parallel β -sheet (highlighted by yellow carbons) spontaneously formed at the surface of the **14** aggregate. Sidechains are not shown so that the backbone H-bonding pattern can be seen. (B) Two views of **14** molecules forming a β -sheet, showing the peptide backbone and Phe sidechains. Similar structures were observed for **12**, albeit with less frequency. (C) Two views of **U** molecules forming a β sheet. Urea- π stacking interactions are prevalent and lead to a distinct backbone conformation including π - π stacking of the Phe sidechains.

4. Studies of PA gelation

To expand their potential biomedical applications, we prepared hydrogels by adding CaCl₂¹⁴ to a PA solution and studied the morphology of the product by scanning electron microscopy (SEM). The formation of hydrogels is triggered by the screening of negatively charged Glu residues by cations. When the cohesive interactions exceed the repulsive forces the PA nanostructures associate each other with the Ca²⁺ cations forming crosslinks. A dense exterior surface is observed in the hydrogels made with **12**, while its interior shows a structure of stacking sheets and an amorphous structure on the crosssection (**Figure 6A** and **Figure S14A**). For hydrogel **14** (**Figure 6B** and **Figure S14B**),

the exterior and interior surfaces are similar, while the surface is more uniform and densely arranged. Meanwhile, an aligned bundle-like structure is observed in hydrogel **U** (**Figure 6C** and **Figure S14C**), which is very different from the other two.

Next, we studied the rigidity of the hydrogels (**Figure 6D**), which showed storage modulus (G') > loss modulus (G") with the strain lower than 10%. The G' for all of these hydrogels is over 10^3 Pa at 1% strain. The linear viscoelastic region of **U** is larger than the other two with the order of **U>12>14**, suggesting higher stability of **U** against mechanic stress. A frequency sweep was then performed and the tan δ (G"/G') was calculated as shown in **Figure S14D**. This parameter provides the ratio of energy observed to energy lost during the viscous deformation. During the test, $\tan(\delta)$ was below 1 at all frequencies, which means the samples behave more like an elastic solid ranging from 0.1 to 100 rad/s. ⁶⁶ Interestingly, a large difference in $\tan(\delta)$ (G"/G') is observed in **14** when compared to **12** and **U**. It has been reported that the bending of the nanofibers can lower the G', ⁵⁶ which suggest that the overall higher and increasing $\tan \delta$ above 10 rad/s of **14** is related to its flat nanosheet structures, as described above. The $\tan(\delta)$ of **12** and **U** are similar, decreasing about 36% and 26% from 0.1 rad/s to the plateau (~3 rad/s). Although **U** has more entanglements than **12** (higher $\tan(\delta)$ at all frequencies), it shows good stability against increasing frequency (experiencing less decreasing to reach the plateau).

Next, we studied the stability of the hydrogel over time by performing a time sweep on a controlled-stress rheometer, which could be related to the self-healing ability of hydrogel. Short Phe-containing peptides have been reported to mimic the self-healing properties of natural tissue,¹⁹ providing high storage modulus due to its strong supramolecular interactions.^{20, 67} **Figure 6E** shows that when a high shear strain (100 %) is applied to the hydrogel, the G' drops to smaller values than the G", indicating the liquefaction of the hydrogel. When the strain is lowered to 0.1% again, G' recovers to be higher than G". These observations demonstrate that the shear-strain disrupted nanofibrous networks can self-heal when the strain is removed. Interestingly, after the removal of 100% strain, U recovers to 47.44% of its original state immediately and reaches 91.89% recovery after 20 mins; 12 immediately recovers to 48.25% and reaches 75.56% after 20 mins, while 14 only recovers to 35.14% immediately and reaches 49.33% after 20 mins. In conclusion, the hydrogel's ability for post-shear recovery is U>12>14. Others have described that

more H-bonds and their closer distance to the core are important to the mechanical properties of the gel.¹³ It has been recently reported that increased H-bonding can enhance the toughness of individual PA nanofibers and their hydrogels.⁵⁶ The extra H-bonds supplied by urea make the connection among fibers harder to break and easily to reform under strain. In summary, the urea motif affects the mechanical properties (stability against mechanical stress and ability for shear recovery) of the hydrogel due to its stronger H-bonds, flexible bending morphology, and non-cross-linking structures in the gel.

To further evaluate the self-healing ability of the hydrogels, we performed a macroscopic self-healing test (**Figure S15**). Two hydrogels were made for each sample and one of them was stained with Trypan Blue. The hydrogels were all cut into 2 pieces, and then the broken hydrogels were combined into dyed/non-dyed pairs. After 20 mins at room temperature, a significant blue color spreading can be observed (not shown) and after 15 hours the boundaries between the different colored pieces turned obscure (**Figure S15 A-B**). This indicates the self-healing ability due to the existence of dynamic covalent bonds in the hydrogel network.⁶⁸

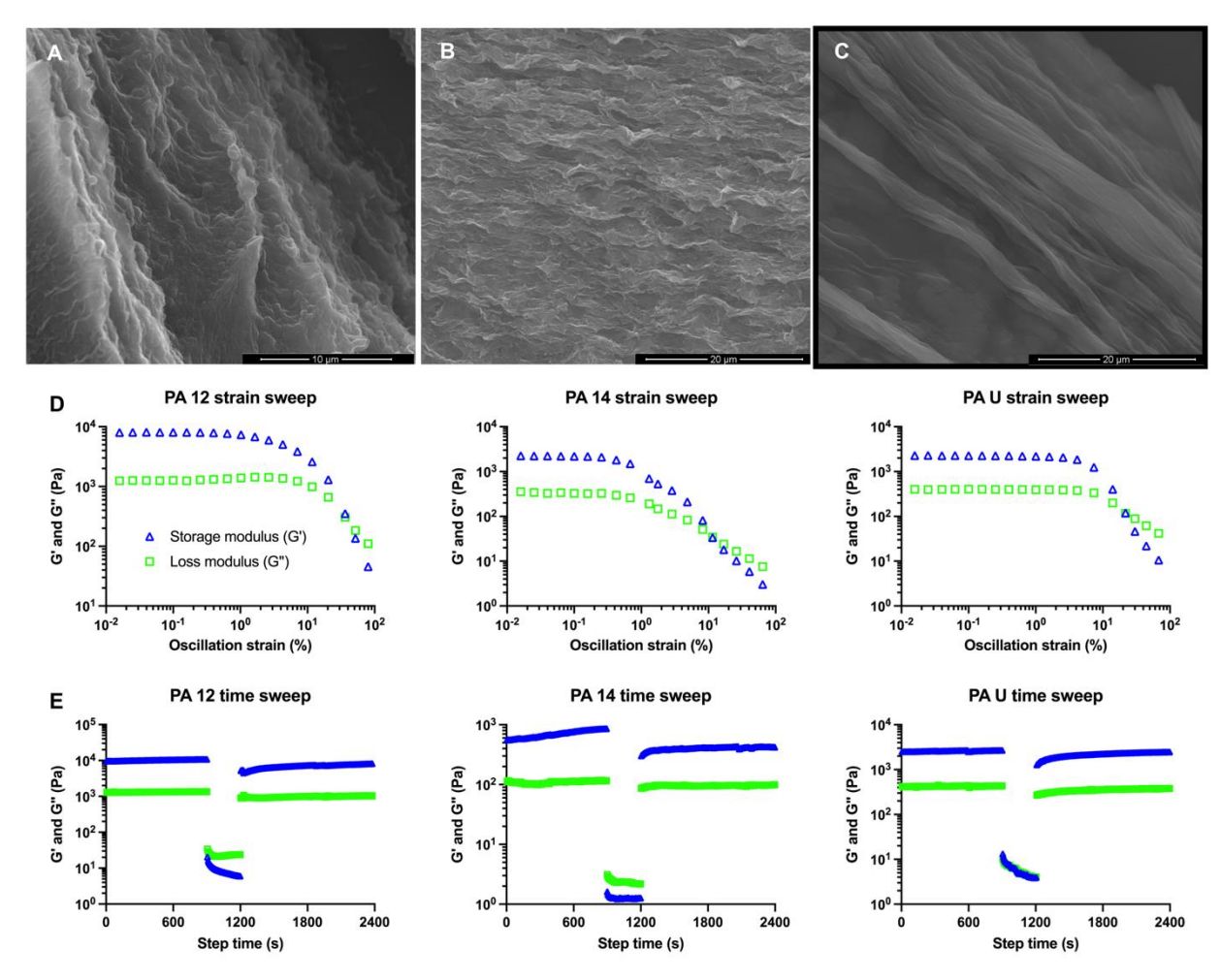


Figure 6. Characterization of the PA hydrogels. **A-C**) SEM images of **PA 12, 14,** and **U**, from left to right, respectively. **D**) Strain sweep performed after gelation with Ca^{2+} shows the hydrogel formation, indicating by G' > G'' with a strain less than 10%. **E**) Time sweep performed over 40 mins. Hydrogel is allowed to equilibrate at a constant frequency of 10 rad/s and 0.1% strain for 15 mins, as the shear increases to 100% for 5 min, the G' drops notably. After removal of the strain, the G' increases over 20 mins. The interval between each measurement is 7 seconds, which is the minimum time interval that can be get from the instrument used here.

5. Metabolism and cytotoxicity studies

To achieve a biomedical application, it is key to determine the metabolic stability and biocompatibility of PA nanostructures. As shown in **Figure 7**, serum metabolism was studied by monitoring the PAs after they had been incubated with serum for 24 h. All PAs are stable in serum (>80% remaining after 180 mins incubation and >75% after 1440 mins) as shown in **Figure 7A**.

Next, we tested the cell viability of both PA solutions and PA gels. HaCaT and SH-SY5Y cell lines were selected for biological-related assays as both of them have been extensively used to study toxicology and 3D cell cultures. Additionally, HaCaT cells are immortalized human keratinocytes that may indicate the use of the hydrogels in wound repair. Meanwhile, SH-SY5Y cells are a human neuroblastoma cell line that are commonly used to study adhesion and spreading patterns. The PAs are not toxic at 100 μg/mL solution toward HaCaT and SH-SY5Y cell lines as shown in Figure 7B for 100 µg/mL and for higher concentrations (5 mg/mL and 10 mg/mL) in Figure S16. The cytotoxicity of PA hydrogels (10 mg/mL) was then studied to assess a potential biomaterial application by measuring the release of lactate dehydrogenase (LDH) after 24 h incubation (Figure 7C, D). Though the differences among the cytotoxicities of these three hydrogels are not significant, there is a slightly smaller cell viability with 14 after 24 h incubation. Interestingly, **14** has the highest cell viability in solution at 100 μg/mL. This discrepancy may be caused by the alteration of the interplay between hydrophobic and electrostatic interactions in the gelation process. It has been demonstrated that for PA hydrogel culturing, parameters such as charge, hydrophobicity, and strong intermolecular cohesion influence cell viability. 17 In this case, the charges are not a consideration as they are screened by the salt during the gelation. 14 has the strongest hydrophobicity (LogP 20% greater than **U** and 32% greater than **12**), calculated by mol inspiration.⁶⁹ A longer alkyl tail (strong hydrophobicity) is considered as one of the possible reasons for cell death caused by inserting, interacting, and thus disrupting the cell membranes.⁴⁶ Furthermore, **14** seems to have less cohesion when the salt concentration is increased. The width of nanostructure 14 decreased more than 200% when the salt concentration was increased from 17.5 mM to 35 mM (data not shown, the effect of salt to be reported later). Another clue is that the hydrogel 14 disassembled more easily than the other two PAs from fibrous structures to aggregates in cell medium (see confocal images in Figure ??). These observations validate the report from Stupp's lab stating that weaker intermolecular bonds promote cell death.¹⁷ Finally, though **U** is more hydrophobic than 12, they are similar in cell viability support as it is expected that U has stronger intermolecular cohesion due to the extra H-bond.

Confocal microscopy was performed to visualize the dead/alive cells incubated with PA gels by Dil (cell membrane) and Calcein (viability) staining. To avoid dye encapsulation inside the PAs, the cells were stained alone for 15 mins and then seeded on PA-coated surfaces (details shown in SI and **Figure S17A**) and images taken after 4 h of incubation. Good cell membrane integrity (Dil, orange) and viability (Calcein, green) were observed in all the PAs in two cell lines (SH-SY5Y, **Figure 7E** and HaCaT, **Figure S17B**).

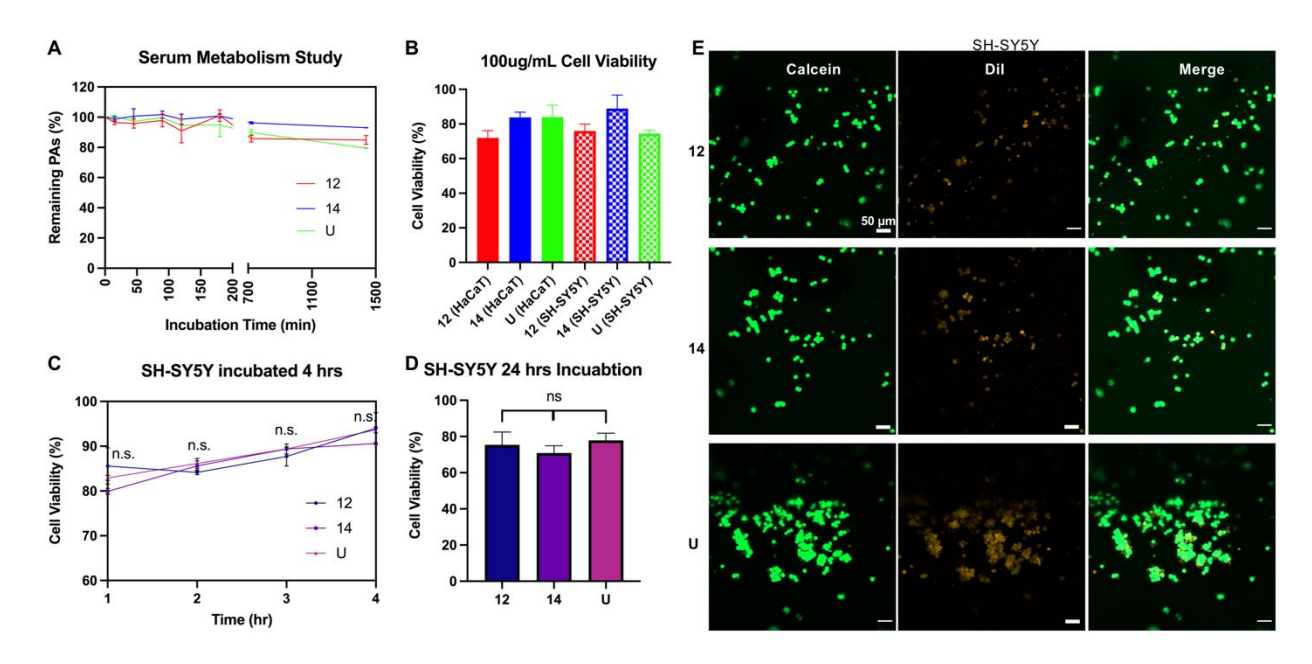


Figure 7. A) PA's stability in serum and **B-E**) cytotoxicity of HaCaT and SH-SY5Y cell lines. **A)** Remaining PAs after 24 h incubation with 50% v/v serum at 37°C. **B)** Viability of HaCaT and SH-SY5Y cell lines incubated with 100 μg/mL PA solutions after 24 h. The cell viability measured by LDH release of SH-SY5Y cells after incubation with the PA hydrogels (10 mg/mL) for **C)** 4 h and **D)** 24 h. **E)** Confocal images of SH-SY5Y stained by Dil/Calcein. The cells were stained alone and then seeded on the PA gels. The images were taken after 4 h incubation. The orange color indicated the Dil stained cell membranes and the green color indicated the Calcein stained live cells. Scale bar 50 μm.

6. Cell culture

We studied the cell adhesion and spreading of SH-SY5Y cells on PA-coated surfaces after 48 h to assess the potency of these three gels to serve as a 2D culture matrix. We determined the cell morphology by spreading area and cell circularity at 24 h post-seeding. The circularity was calculated as $(4\pi \times \text{surface area})/(\text{perimeter})^2$. SH-SY5Y cells were able to attach and spread on all three hydrogels (**Figure 8D**). However, significant differences can be observed in the spreading area and cell shape (determined by

circularity). More elongated cells and larger spreading areas were found with **U** than the other two (**Figure 8B** and **C**, with more details shown in **Figure S18**). It has been reported that stiffness, ⁵⁶ nanofibrous structure, ²² and fibrous density ⁷⁰ of the hydrogels relate to the ability to support cell adhesion and spreading. The three gels can be considered as "soft" matrix (in a range 0.5-10 kPa stiffness) for cell culture. ⁷¹ Although they possess similar gel stiffness, the aligned bundle-like structures of **U** (**Figure 6**) supported cell spreading better than the other gels (which seem to have high porosity and less nanofibrous structures). In conclusion, the data suggest that SH-SY5Y cells can attach and spread well on our hydrogel surfaces with hydrogel **U** behaving better in supporting cell spreading than the other two.

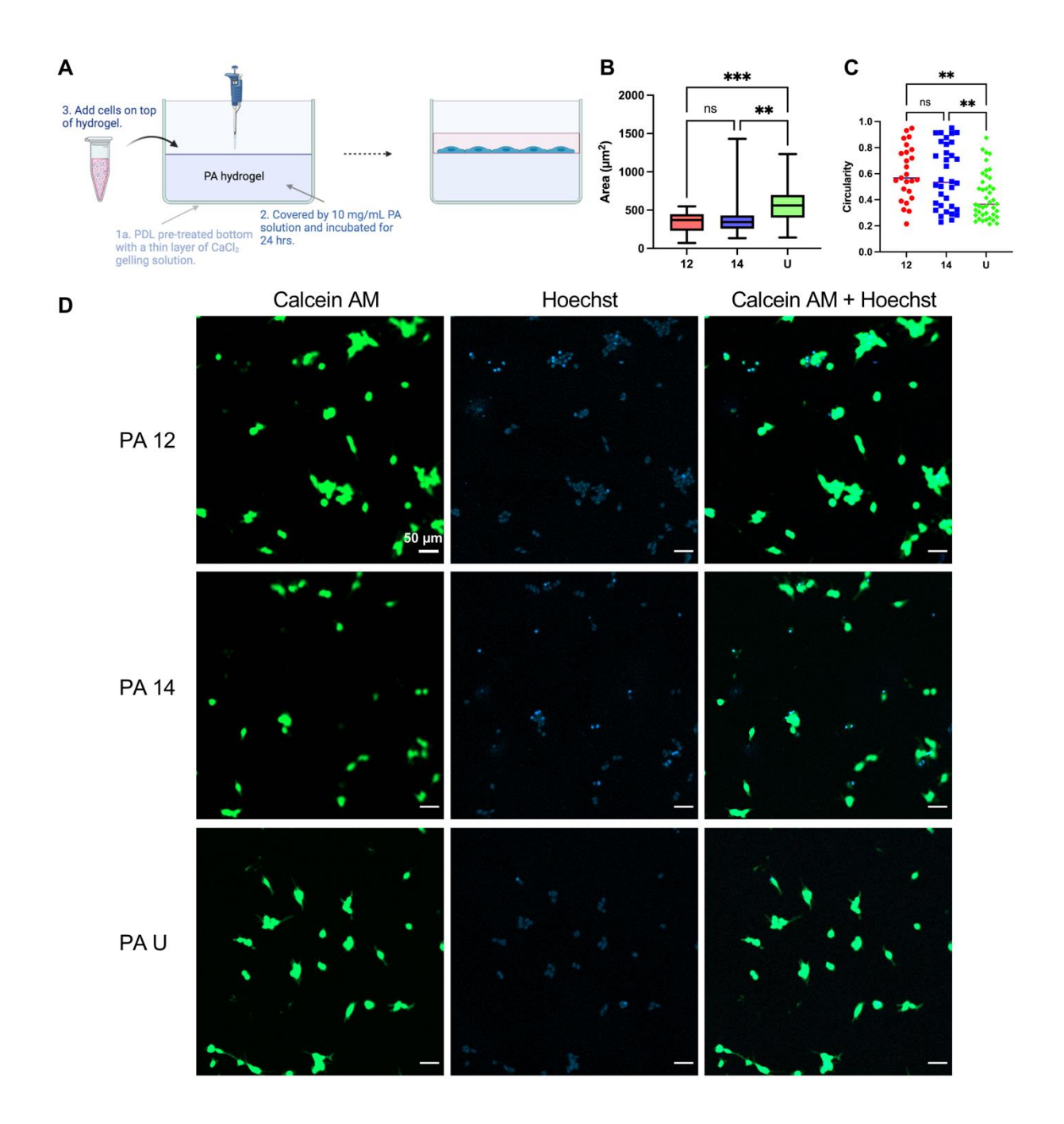


Figure 8. **A)** Schematic depicting the procedure for SH-SY5Y cell line by 2D cell culture. The plate was treated with Poly-D-Lysine (PDL) and covered by a thin layer of PA gel made with CaCl₂ solution. SH-SY5Y cells were cultured on the PA-coating surface for 48 h. **B)** Quantitative analysis of spreading area (*** P < 0.001) and **C)** circularity (** P < 0.01) of SH-SY5Y cells using Image J software. One-way ANOVA with Tukey post-test was used for comparisons. **12** and **14** have similar abilities to support cell adhesion and spreading, while **U** shows a significantly better ability. **D)** Respective confocal images of SH-SY5Y cells culturing on PA gels for 48h. Scale bar 50 μm. Cells were stained by Calcein (green, alive) and Hoechst 33342 (blue, nuclear).

Then, we studied the suitability of these hydrogels for 3D culturing of SH-SY5Y and HaCaT cell lines. We used two different protocols to prepare the PA-cell constructs. In the first strategy we formed two layers of hydrogels to build up a 3D matrix (**Figure 9A**). Cell substrates such as collagen^{17, 18}, sodium alginate,¹⁷ and agarose⁷² have been used together with peptides to form a robust hybrid hydrogel to achieve better 3D performance. Thus, a thin layer of agarose gel was used to coat the bottom of the plate, and then a PA-cell solution was added on the top to form the second gel layer. The SH-SY5Y cells were stained by calcein and Hoechst (cell live/dead reporter) and imaged after 48 h of incubation (see **Figure 9B**). Multilayered cell distributions can be observed from the z-stack images (not shown here). These data suggest the feasibility of these hydrogels to serve as a cell culture matrix.

The second cell encapsulation method is to form an oriented PA scaffolds (details shown in SI). It has been reported that the degree of cell alignment can be enhanced with oriented PA scaffolds while decreasing when the cell density increases (longer incubation time). 18 Thus, we incubated HaCaT cells with the second gelation method to study the behavior of our three PA hydrogels in cell culture. As shown in Figure S19B, after 5 d of incubation, some cells escaped from the PA scaffold. One of the reasons to explain the decreasing cell accessibility to the PA scaffold is that cell activity and growth in the media induced PA scaffold remodeling. 18 Further, more cells were observed inside the gels of 12 and U than inside 14. We hypothesized that this happens because a more stable PA hydrogel in the growth medium results in better cell accessibility. To test this hypothesis, we stain the PA-cell hydrogels with calcein and propidium podide (PI). On day 1, fibrous structures were observed in all PA gels. Interestingly, on day 5, only the fibrous structures can still be found in hydrogel **U**, while the coexistence of fibrous and large aggregates was found in hydrogel 12 and only small petaloid particles are observed for hydrogel 14 (images shown in Figure S20). It is clear the urea motif increases the structural stability maintaining the fibrous shape during cell culturing, as the fibrous shape is a key factor for the hydrogel to function as cell growth matrix. These observations are consistent with the lower cell viability obtained from LDH release measurement with hydrogel 14 discussed above, which provides us with another explanation. In conclusion, the three PAs can work

as cell substrates for 3D culture, with the hydrogel of ${\bf U}$ being most stable during the cell		
growth process.		

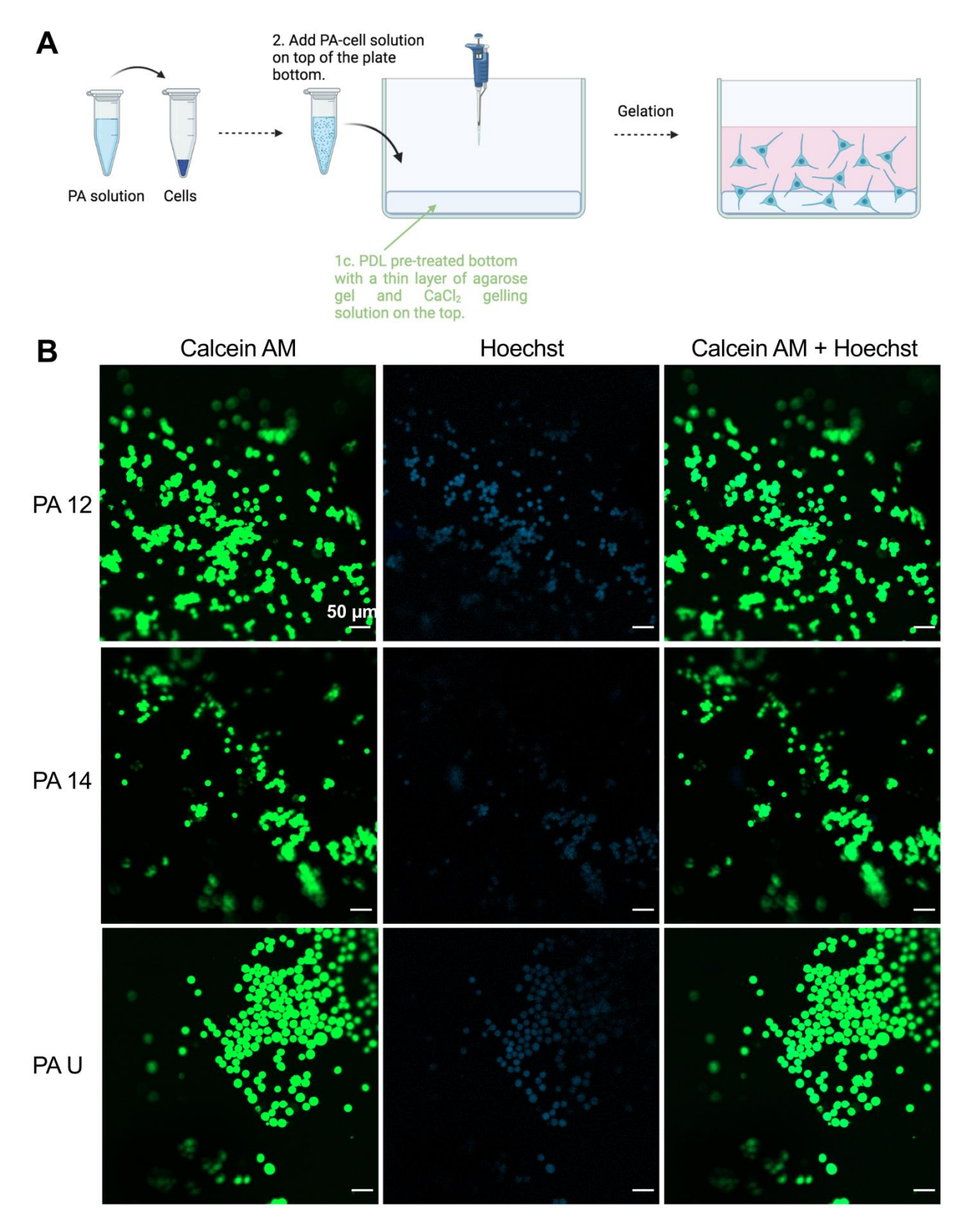


Figure 9. **A)** Schematic depicting the procedure for SH-SY5Y by 3D cell culture. The plate was treated first with PDL and then covered by a thin layer of agarose gel. Then a second gel layer, PA-cell gel was made

on the top, thus encapsulating the cells inside the PA scaffold. **B**) The confocal fluorescent images show calcein AM (green) and Hoechst (blue) cell staining inside the 3D gel matrix, after 48 h incubation. Scale bar 50 μ m. The blue dots in the right panel are not clear to see because of the low number of dead cells and the high saturation of green color.

Conclusion

To develop PAs that can be customized for specific biomedical applications, it is crucial to understand and exploit the interplay of the small forces that determine the morphology, size, and functionality of the nanostructures. We have demonstrated that adding a urea motif (stronger H-bonding) alters the supramolecular morphology of PA nano-assemblies in an aqueous solution. The urea group also affects the internal arrangement of the nanostructures. The IR, CD, and LD data indicate differences in H-bonding patterns and suggest differences in the intramolecular interactions, possibly due to urea— π stacking. A stable (independent of time and pathlength) internal structure was also obtained from the urea-modified PA. SAXS and NMR suggest the higher compactness with the ureamodified PA nanostructures. Computer simulations indicate that the urea motif contributes an increased number of H-bonds to the nanostructure and forms urea-π interactions with the Phe side chain. These interactions alter the backbone conformation of the PA and are likely responsible for the distinct morphology of the urea-linked PA seen at larger scales. We further showed that the hydrogel made of urea-modified PA has the best stability against mechanistic stress and self-healing ability than its counterparts. The resulting hydrogel supports cell adhesion and spreading on its surface, while possessing good stability to entrap cells during long-time cell culturing. In summary, the inclusion of urea in PAs is a viable option to create supramolecular assemblies with ideal morphology for self-healing and use as a cell growth matrix.

ASSOCIATED CONTENT

Supporting Information

The Supporting Information is available free of charge at

Preparation and molecular dynamic protocols. Characterization of the PA nanostructures and assessment of supramolecular shape. SAXS and NMR studies. CD and gelation studied. Cell experiments.

AUTHOR INFORMATION

Corresponding Author

*Martin Conda-Sheridan

Email: martin.condasheridan@unmc.edu;

Phone: +1 402-559-9361

Authors

Huihua Xing 0000-0001-7276-6601

Alison Rodger 0000-0002-7111-3024

Jeffrey Comer 0000-0003-4437-1260

Cristián Huck-Iriart 0000-0001-5734-2499; Current Address: ALBA Synchrotron Light

Source, Carrer de la Llum 2-26, Cerdanyola del Vallès, 08290 Barcelona, Spain

Agustín S. Picco 0000-0003-4683-7319

Martin Conda-Sheridan 0000-0002-3568-2545

Author Contributions

M.C.-S. conceived the idea, supervised the experiments, and undertook data analysis.

H.X. performed PA synthesis, samples preparation, CD, TEM, AFM, SEM, SAXS,

rheometry, biological assays, and cell culture experimental. A.R. collected and analyzed

CD, LD, and FTIR data. J.C. designed the computational model, analyzed, and

interpreted the results. C.H.-I. and A.S.P. analyzed SAXS and contributed to the overall

idea. E.L.E. performed and analyzed the NMR NOESY. The manuscript was written

through the contributions of all authors. All authors have given approval to the final version

of the manuscript.

Notes

The authors declare no competing financial interest.

ACKNOWLEDGMENTS

MC-S acknowledges support from the National Science Foundation (NSF) CAREER Award (DMR-1941731). HX thanks for the support from the UNMC fellowship. JC's contribution is based on work supported by the National Science Foundation (DMR-1945589). A majority of the computing was performed on the Beocat Research Cluster at Kansas State University, which has been funded in part by the NSF (CHE-1726332). SAXS work was performed at the Center for High Energy X-ray Sciences (CHEXS) supported by the NSF under award DMR-1829070 using the Macromolecular Diffraction at CHESS (MacCHESS) facility, which is supported by NIGMS award 1-P30-GM124166-01A1 and NYSTAR (Richard Gillilan and Qinggiu Huang). The authors appreciate Luana J. de Campos and Aramis J. Pereira at UNMC for helping with the sample preparation for SAXS. The authors further acknowledge NCI funding of the Eppley NMR Core facility and thank the Electron Microscopy Core Facility (Tom Bargar and Nicholas Conoan), Nanoimaging Core Facility (Alexander Lushnikov), and Advanced Microscopy Core Facility (Janice A. Taylor and James R. Talaska) at UNMC for experimental assistance. A.S.P and C.H.I are staff members of CONICET and acknowledge its support. A.S.P. acknowledge UNLP and C.H.I UNSAM for their support.

REFERENCES

- 1. Sato, K.; Hendricks, M. P.; Palmer, L. C.; Stupp, S. I., Peptide supramolecular materials for therapeutics. Chem. Soc. Rev. **2018**, 47 (20), 7539-7551.
- 2. Clemons, T. D.; Stupp, S. I., Design of materials with supramolecular polymers. Prog. Polym. Sci. **2020**, 111, 101310.
- 3. Dumele, O.; Chen, J.; Passarelli, J. V.; Stupp, S. I., Supramolecular Energy Materials. Adv. Mater. **2020**, 32 (17), 1907247.
- 4. Hendricks, M. P.; Sato, K.; Palmer, L. C.; Stupp, S. I., Supramolecular Assembly of Peptide Amphiphiles. Acc. Chem. Res. **2017**, 50 (10), 2440-2448.
- 5. Hamley, I. W., Self-assembly of amphiphilic peptides. Soft Matter **2011,** 7 (9), 4122-4138.
- 6. Versluis, F.; Marsden, H. R.; Kros, A., Power struggles in peptide-amphiphile nanostructures. Chem. Soc. Rev. **2010**, 39 (9), 3434-3444.
- 7. Cui, H.; Webber, M. J.; Stupp, S. I., Self-assembly of peptide amphiphiles: from molecules to nanostructures to biomaterials. Biopolymers **2010**, 94 (1), 1-18.

- 8. Levin, A.; Hakala, T. A.; Schnaider, L.; Bernardes, G. J. L.; Gazit, E.; Knowles, T. P. J., Biomimetic peptide self-assembly for functional materials. Nat. Rev. Chem. **2020**, 4 (11), 615-634.
- 9. Kulkarni, K.; Habila, N.; Del Borgo, M. P.; Aguilar, M.-I., Novel Materials From the Supramolecular Self-Assembly of Short Helical $\beta(3)$ -Peptide Foldamers. Front. Chem. **2019**, 7, 70-70.
- 10. Edwards-Gayle, C. J. C.; Hamley, I. W., Self-assembly of bioactive peptides, peptide conjugates, and peptide mimetic materials. Org. Biomol. Chem. **2017**, 15 (28), 5867-5876.
- 11. Acar, H.; Srivastava, S.; Chung, E. J.; Schnorenberg, M. R.; Barrett, J. C.; LaBelle, J. L.; Tirrell, M., Self-assembling peptide-based building blocks in medical applications. Adv. Drug Deliv. Rev. **2017**, 110-111, 65-79.
- 12. Dehsorkhi, A.; Castelletto, V.; Hamley, I. W., Self-assembling amphiphilic peptides. J. Pept. Sci. **2014**, 20 (7), 453-467.
- 13. Paramonov, S. E.; Jun, H.-W.; Hartgerink, J. D., Self-Assembly of Peptide–Amphiphile Nanofibers: The Roles of Hydrogen Bonding and Amphiphilic Packing. J. Am. Chem. Soc. **2006**, 128 (22), 7291-7298.
- 14. Pashuck, E. T.; Cui, H.; Stupp, S. I., Tuning Supramolecular Rigidity of Peptide Fibers through Molecular Structure. J. Am. Chem. Soc. **2010**, 132 (17), 6041-6046.
- 15. Jiang, H.; Guler, M. O.; Stupp, S. I., The internal structure of self-assembled peptide amphiphiles nanofibers. Soft Matter **2007**, 3 (4), 454-462.
- 16. Hung, A. M.; Stupp, S. I., Understanding Factors Affecting Alignment of Self-Assembling Nanofibers Patterned by Sonication-Assisted Solution Embossing. Langmuir **2009**, 25 (12), 7084-7089.
- 17. Newcomb, C. J.; Sur, S.; Ortony, J. H.; Lee, O.-S.; Matson, J. B.; Boekhoven, J.; Yu, J. M.; Schatz, G. C.; Stupp, S. I., Cell death versus cell survival instructed by supramolecular cohesion of nanostructures. Nat. Commun. **2014**, 5 (1), 3321.
- 18. Bakota, E. L.; Wang, Y.; Danesh, F. R.; Hartgerink, J. D., Injectable Multidomain Peptide Nanofiber Hydrogel as a Delivery Agent for Stem Cell Secretome. Biomacromolecules **2011**, 12 (5), 1651-1657.
- 19. Choe, R.; Il Yun, S., Fmoc-diphenylalanine-based hydrogels as a potential carrier for drug delivery. e-Polymers **2020**, 20 (1), 458-468.
- 20. Xie, Y.; Zhao, J.; Huang, R.; Qi, W.; Wang, Y.; Su, R.; He, Z., Calcium-Ion-Triggered Co-assembly of Peptide and Polysaccharide into a Hybrid Hydrogel for Drug Delivery. Nanoscale Res. Lett. **2016**, 11 (1), 184.
- 21. Goktas, M.; Cinar, G.; Orujalipoor, I.; Ide, S.; Tekinay, A. B.; Guler, M. O., Self-Assembled Peptide Amphiphile Nanofibers and PEG Composite Hydrogels as Tunable ECM Mimetic Microenvironment. Biomacromolecules **2015**, 16 (4), 1247-1258.
- 22. Jacob, R. S.; Ghosh, D.; Singh, P. K.; Basu, S. K.; Jha, N. N.; Das, S.; Sukul, P. K.; Patil, S.; Sathaye, S.; Kumar, A.; Chowdhury, A.; Malik, S.; Sen, S.; Maji, S. K., Self healing hydrogels composed of amyloid nano fibrils for cell culture and stem cell differentiation. Biomaterials **2015**, 54, 97-105.
- 23. Jayawarna, V.; Ali, M.; Jowitt, T. A.; Miller, A. F.; Saiani, A.; Gough, J. E.; Ulijn, R. V., Nanostructured Hydrogels for Three-Dimensional Cell Culture Through Self-Assembly of Fluorenylmethoxycarbonyl—Dipeptides. Adv. Mater. **2006**, 18 (5), 611-614.

- 24. Stendahl, J. C.; Rao, M. S.; Guler, M. O.; Stupp, S. I., Intermolecular Forces in the Self-Assembly of Peptide Amphiphile Nanofibers. Adv. Funct. Mater. **2006**, 16 (4), 499-508.
- 25. Goyal, S.; Chattopadhyay, A.; Kasavajhala, K.; Priyakumar, U. D., Role of Urea–Aromatic Stacking Interactions in Stabilizing the Aromatic Residues of the Protein in Urea-Induced Denatured State. J. Am. Chem. Soc. **2017**, 139 (42), 14931-14946.
- 26. Coe, S.; Kane, J. J.; Nguyen, T. L.; Toledo, L. M.; Wininger, E.; Fowler, F. W.; Lauher, J. W., Molecular Symmetry and the Design of Molecular Solids: The Oxalamide Functionality as a Persistent Hydrogen Bonding Unit. J. Am. Chem. Soc. **1997**, 119 (1), 86-93.
- 27. Kane, J. J.; Liao, R.-F.; Lauher, J. W.; Fowler, F. W., Preparation of layered diacetylenes as a demonstration of strategies for supramolecular synthesis. J. Am. Chem. Soc. **1995**, 117 (48), 12003-12004.
- 28. Zhao, X.; Chang, Y. L.; Fowler, F. W.; Lauher, J. W., An approach to the design of molecular solids. The ureylene dicarboxylic acids. J. Am. Chem. Soc. **1990**, 112 (18), 6627-6634.
- 29. Fong, C.; Wells, D.; Krodkiewska, I.; Hartley, P. G.; Drummond, C. J., New Role for Urea as a Surfactant Headgroup Promoting Self-Assembly in Water. Chem. Mater. **2006**, 18 (3), 594-597.
- 30. Tosi, F.; Berrocal, J. A.; Stuart, M. C. A.; Wezenberg, S. J.; Feringa, B. L., Tuning of Morphology by Chirality in Self-Assembled Structures of Bis(Urea) Amphiphiles in Water. Chem. Eur. J. **2021**, 27 (1), 326-330.
- 31. Dawei, Z.; Tie, Z.; Chunmei, L.; Qin, M.; Lu, X.; Wang, M.; Wang, W.; Chen, P., Effects of Hydrophobicity and Anions on Self-Assembly of the Peptide EMK16-II. Biopolymers **2009**, 93, 318-29.
- 32. Fleming, S.; Ulijn, R. V., Design of nanostructures based on aromatic peptide amphiphiles. Chem. Soc. Rev. **2014**, 43 (23), 8150-8177.
- 33. Scott, G.; Roy, S.; Abul-Haija, Y. M.; Fleming, S.; Bai, S.; Ulijn, R. V., Pickering Stabilized Peptide Gel Particles as Tunable Microenvironments for Biocatalysis. Langmuir **2013**, 29 (46), 14321-14327.
- 34. Yang, Z.; Liang, G.; Wang, L.; Xu, B., Using a Kinase/Phosphatase Switch to Regulate a Supramolecular Hydrogel and Forming the Supramolecular Hydrogel in Vivo. J. Am. Chem. Soc. **2006**, 128 (9), 3038-3043.
- 35. Lee, J.; Ju, M.; Cho, O. H.; Kim, Y.; Nam, K. T., Tyrosine-Rich Peptides as a Platform for Assembly and Material Synthesis. Adv. Sci. **2019**, 6 (4), 1801255.
- 36. Partlow, B. P.; Bagheri, M.; Harden, J. L.; Kaplan, D. L., Tyrosine Templating in the Self-Assembly and Crystallization of Silk Fibroin. Biomacromolecules **2016**, 17 (11), 3570-3579.
- 37. German, H. W.; Uyaver, S.; Hansmann, U. H. E., Self-Assembly of Phenylalanine-Based Molecules. J. Phys. Chem. A **2015**, 119 (9), 1609-1615.
- 38. Tomar, D.; Chaudhary, S.; Jena, K. C., Self-assembly of I-phenylalanine amino acid: electrostatic induced hindrance of fibril formation. RSC Advances **2019**, 9 (22), 12596-12605.
- 39. Aida, T.; Meijer, E. W.; Stupp, S. I., Functional Supramolecular Polymers. Science **2012**, 335 (6070), 813.

- 40. Pashuck, E. T.; Stupp, S. I., Direct Observation of Morphological Tranformation from Twisted Ribbons into Helical Ribbons. J. Am. Chem. Soc. **2010**, 132 (26), 8819-8821.
- 41. Childers, W. S.; Mehta, A. K.; Ni, R.; Taylor, J. V.; Lynn, D. G., Peptides Organized as Bilayer Membranes. Angew. Chem. Int. Ed. **2010**, 49 (24), 4104-4107.
- 42. Cui, H.; Muraoka, T.; Cheetham, A. G.; Stupp, S. I., Self-Assembly of Giant Peptide Nanobelts. Nano Lett. **2009**, 9 (3), 945-951.
- 43. Hatip Koc, M.; Cinar Ciftci, G.; Baday, S.; Castelletto, V.; Hamley, I. W.; Guler, M. O., Hierarchical Self-Assembly of Histidine-Functionalized Peptide Amphiphiles into Supramolecular Chiral Nanostructures. Langmuir **2017**, 33 (32), 7947-7956.
- 44. Arslan, E.; Hatip Koc, M.; Uysal, O.; Dikecoglu, B.; Topal, A. E.; Garifullin, R.; Ozkan, A. D.; Dana, A.; Hermida-Merino, D.; Castelletto, V.; Edwards-Gayle, C.; Baday, S.; Hamley, I.; Tekinay, A. B.; Guler, M. O., Supramolecular Peptide Nanofiber Morphology Affects Mechanotransduction of Stem Cells. Biomacromolecules **2017**, 18 (10), 3114-3130.
- 45. Reddy, L. S.; Basavoju, S.; Vangala, V. R.; Nangia, A., Hydrogen Bonding in Crystal Structures of N,N'-Bis(3-pyridyl)urea. Why Is the N-H···O Tape Synthon Absent in Diaryl Ureas with Electron-Withdrawing Groups? Cryst. Growth Des. **2006**, 6 (1), 161-173.
- 46. Rodrigues de Almeida, N.; Han, Y.; Perez, J.; Kirkpatrick, S.; Wang, Y.; Sheridan, M. C., Design, Synthesis, and Nanostructure-Dependent Antibacterial Activity of Cationic Peptide Amphiphiles. ACS Appl. Mater. Inter. **2018**, 11, 2790.
- 47. Zaldivar, G.; Vemulapalli, S.; Udumula, V.; Conda-Sheridan, M.; Tagliazucchi, M., Self-Assembled Nanostructures of Peptide Amphiphiles: Charge Regulation by Size Regulation. J. Phys. Chem. C **2019**, 123 (28), 17606-17615.
- 48. Marrington, R.; Dafforn, T. R.; Halsall, D. J.; Hicks, M.; Rodger, A., Validation of new microvolume Couette flow linear dichroism cells. Analyst **2005**, 130, 1608-1616.
- 49. Burnett, E. K.; Ai, Q.; Cherniawski, B. P.; Parkin, S. R.; Risko, C.; Briseno, A. L., Even–Odd Alkyl Chain-Length Alternation Regulates Oligothiophene Crystal Structure. Chem. Mater. **2019**, 31 (17), 6900-6907.
- 50. Yuan, L.; Thompson, D.; Cao, L.; Nerngchangnong, N.; Nijhuis, C. A., One Carbon Matters: The Origin and Reversal of Odd–Even Effects in Molecular Diodes with Self-Assembled Monolayers of Ferrocenyl-Alkanethiolates. J. Phys. Chem. C **2015**, 119 (31), 17910-17919.
- 51. Arbely, E.; Rutherford, T. J.; Neuweiler, H.; Sharpe, T. D.; Ferguson, N.; Fersht, A. R., Carboxyl pKa Values and Acid Denaturation of BBL. J. Mol. Biol. **2010**, 403 (2), 313-327.
- 52. Friedrich, H.; Frederik, P. M.; de With, G.; Sommerdijk, N. A. J. M., Imaging of Self-Assembled Structures: Interpretation of TEM and Cryo-TEM Images. Angew. Chem. Int. Ed. **2010**, 49 (43), 7850-7858.
- 53. Mammadov, R.; Tekinay, A. B.; Dana, A.; Guler, M. O., Microscopic characterization of peptide nanostructures. Micron **2012**, 43 (2), 69-84.
- 54. Sarroukh, R.; Cerf, E.; Derclaye, S.; Dufrêne, Y. F.; Goormaghtigh, E.; Ruysschaert, J.-M.; Raussens, V., Transformation of amyloid $\beta(1-40)$ oligomers into fibrils is characterized by a major change in secondary structure. Cell. Mol. Life Sci. **2011**, 68 (8), 1429-1438.

- 55. Waeytens, J.; Van Hemelryck, V.; Deniset-Besseau, A.; Ruysschaert, J.-M.; Dazzi, A.; Raussens, V., Characterization by Nano-Infrared Spectroscopy of Individual Aggregated Species of Amyloid Proteins. Molecules **2020**, 25 (12).
- 56. Godbe, J. M.; Freeman, R.; Lewis, J. A.; Sasselli, I. R.; Sangji, M. H.; Stupp, S. I., Hydrogen Bonding Stiffens Peptide Amphiphile Supramolecular Filaments by Aza-Glycine Residues. Acta Biomater. **2021**, 135, 87-99.
- 57. Bulheller, B. M.; Rodger, A.; Hicks, M. R.; Dafforn, T. R.; Serpell, L. C.; Marshall, K. E.; Bromley, E. H. C.; King, P. J. S.; Channon, K. J.; Woolfson, D. N.; Hirst, J. D., Flow Linear Dichroism of Some Prototypical Proteins. J. Am. Chem. Soc. **2009**, 131 (37), 13305-13314.
- 58. Chen, L.; Morris, K.; Laybourn, A.; Elias, D.; Hicks, M. R.; Rodger, A.; Serpell, L.; Adams, D. J., Self-Assembly Mechanism for a Naphthalene-Dipeptide Leading to Hydrogelation. Langmuir **2010**, 26 (7), 5232-5242.
- 59. Dafforn, T. R.; Rajendra, J.; Halsall, D. J.; Serpell, L. C.; Rodger, A., Protein Fiber Linear Dichroism for Structure Determination and Kinetics in a Low-Volume, Low-Wavelength Couette Flow Cell. Biophys. J. **2004**, 86 (1), 404-410.
- 60. Marshall, K. E.; Hicks, M. R.; Williams, T. L.; Hoffmann, S. V.; Rodger, A.; Dafforn, T. R.; Serpell, L. C., Characterizing the assembly of the Sup35 yeast prion fragment, GNNQQNY: structural changes accompany a fiber-to-crystal switch. Biophys. J. **2010**, 98 (2), 330-338.
- 61. Tamamis, P.; Adler-Abramovich, L.; Reches, M.; Marshall, K.; Sikorski, P.; Serpell, L.; Gazit, E.; Archontis, G., Self-assembly of phenylalanine oligopeptides: insights from experiments and simulations. Biophys. J. **2009**, 96 (12), 5020-5029.
- 62. Rodger, A.; Rajendra, J.; Marrington, R.; Ardhammar, M.; Nordén, B.; Hirst, J. D.; Gilbert, A. T. B.; Dafforn, T. R.; Halsall, D. J.; Woolhead, C. A.; Robinson, C.; Pinheiro, T. J. T.; Kazlauskaite, J.; Seymour, M.; Perez, N.; Hannon, M. J., Flow
- oriented linear dichroism to probe protein orientation in membrane environments. Phys. Chem. **2002**, 4 (16), 4051-4057.
- 63. Radak, B. K.; Chipot, C.; Suh, D.; Jo, S.; Jiang, W.; Phillips, J. C.; Schulten, K.; Roux, B., Constant-pH Molecular Dynamics Simulations for Large Biomolecular Systems. J. Chem. Theory Comput. **2017**, 13 (12), 5933-5944.
- 64. Raghunathan, S.; Jaganade, T.; Priyakumar, U. D., Urea-aromatic interactions in biology. Biophys. Rev. **2020**, 12 (1), 65-84.
- 65. Soulages, J. L.; Kim, K.; Walters, C.; Cushman, J. C., Temperature-Induced Extended Helix/Random Coil Transitions in a Group 1 Late Embryogenesis-Abundant Protein from Soybean. Plant Physiol. **2002**, 128 (3), 822.
- 66. Yan, C.; Pochan, D. J., Rheological properties of peptide-based hydrogels for biomedical and other applications. Chem. Soc. Rev. **2010**, 39 (9), 3528-40.
- 67. Zaguri, D.; Shaham-Niv, S.; Chakraborty, P.; Arnon, Z.; Makam, P.; Bera, S.; Rencus-Lazar, S.; Stoddart, P. R.; Gazit, E.; Reynolds, N. P., Nanomechanical Properties and Phase Behavior of Phenylalanine Amyloid Ribbon Assemblies and Amorphous Self-Healing Hydrogels. ACS Appl. Mater. Interfaces **2020**, 12 (19), 21992-22001.
- 68. Wei, Z.; Yang, J. H.; Liu, Z. Q.; Xu, F.; Zhou, J. X.; Zrínyi, M.; Osada, Y.; Chen, Y. M., Novel Biocompatible Polysaccharide-Based Self-Healing Hydrogel. Adv. Funct. Mater. **2015**, 25 (9), 1352-1359.

- 69. https://www.molinspiration.com/cgi-bin/properties. **2022**.
- 70. Black, K. A.; Lin, B. F.; Wonder, E. A.; Desai, S. S.; Chung, E. J.; Ulery, B. D.; Katari, R. S.; Tirrell, M. V., Biocompatibility and Characterization of a Peptide Amphiphile Hydrogel for Applications in Peripheral Nerve Regeneration. Tissue Eng. Part A **2015**, 21 (7-8), 1333-1342.
- 71. Kruger, T. M.; Bell, K. J.; Lansakara, T. I.; Tivanski, A. V.; Doorn, J. A.; Stevens, L. L., A Soft Mechanical Phenotype of SH-SY5Y Neuroblastoma and Primary Human Neurons Is Resilient to Oligomeric A β (1-42) Injury. ACS Chem. Neurosci. **2020**, 11 (6), 840-850.
- 72. Bergamaschi, G.; Musicò, A.; Frigerio, R.; Strada, A.; Pizzi, A.; Talone, B.; Ghezzi, J.; Gautieri, A.; Chiari, M.; Metrangolo, P.; Vanna, R.; Baldelli Bombelli, F.; Cretich, M.; Gori, A., Composite Peptide–Agarose Hydrogels for Robust and High-Sensitivity 3D Immunoassays. ACS Appl. Mater. Interfaces **2022**, 14 (4), 4811-4822.